RSC Advances

PAPER

View Article Online
View Journal | View Issue

Cite this: *RSC Adv.*, 2025, **15**, 47751

Exploring photocatalytic, thermoelectric, and SLME efficiency of photovoltaic absorber layers for halide double antiperovskites K_6NaAsX_2 (X = Cl, Br, I): a first-principles approach

M. Usman Saeed,[a] Irslan Saeed,[a] Shahan Ali,[a] Ahmed Ali Khan,[a] M. Zia Ur Rehman,[a] Shamiala Pervaiz,[a] Pervaiz Ahmad,[b] Hosam O. Elansary,[c] Sohail Mumtaz *[d] and Y. Saeed *[a]

Received 12th August 2025
Accepted 24th November 2025

DOI: 10.1039/d5ra05938k

rsc.li/rsc-advances

Density functional theory (DFT) was used in this study to examine the structural, electronic, optical, mechanical, thermoelectric, photovoltaic, thermodynamic, and photocatalytic characteristics of double antiperovskite (DAP) compounds K_6NaAsX_2 (where X = Cl, Br, I). In order to optimise lattice parameters and obtain lower bandgaps, first-principles calculations were performed in WIEN2k using the FP-LAPW + LO method with Wu-Cohen GGA (WC–GGA) and the Tran–Blaha modified Becke–Johnson (TB–mBJ) potential. The bandgaps of 1.48 eV, 1.34 eV, and 1.16 eV were found for $K_6NaAsCl_2$, $K_6NaAsBr_2$, and K_6NaAsI_2, respectively, according to band structure investigations using TB–mBJ + SOC. The orbital contributions close to the Fermi level were revealed by the density of states. The optical characteristics, including reflectivity, absorption, extinction coefficient, and refractive index, were computed, while elastic stability creteria confirmed mechanical stability. Thermodynamic properties, including heat capacities, entropy, enthalpy, and Gibbs free energy, were also assessed. Spectroscopic limited maximum efficiency (SLME) analysis revealed promising solar cell efficiency, while photocatalytic results indicated strong oxidizing power suitable for water splitting. Overall, the reduced bandgaps and multifunctional behavior indicate these DAPs as promising candidates for eco-friendly optoelectronic and energy applications.

1. Introduction

Increasing industrialization and using fossil fuels excessively have led to severe environmental pollution and an international energy crisis. In order to combat this, scientists are paying more attention to renewable energy sources, especially solar energy, owing to its environmental advantages and sustainability.[1–3] Because of their excellent light-absorbing properties and potential to increase power conversion efficiency, perovskite materials are becoming increasingly popular for use in solar energy applications. As a result, they have become a major focus of ongoing research efforts.[4–6]

Perovskites, ABX_3, and the crystal structure of $CaTiO_3$ exist in several structural variants, such as antiperovskites (X_3BA) and double perovskites ($A_2B'B''X_6$). These configurations offer distinct advantages, including ease of synthesis and structural stability.[7–9] A recent advancement in this field is emerging double antiperovskites with the formula $X_6B''B'A_2$, which have shown significant potential for diverse technological applications.[10] Hybrid halide perovskites such as $CH_3NH_3PbX_3$ have been extensively studied for high-efficiency solar cells. However, their moisture sensitivity and lead toxicity remain major drawbacks. To overcome these issues, researchers have turned to stable, lead-free alternatives such as halide double perovskites Cs_2AgBiX_6 (X = Cl, Br, I). Hybrid halide perovskites such as $CH_3NH_3PbX_3$ have been extensively studied for high-efficiency solar cells. However, their moisture sensitivity and lead toxicity remain major drawbacks. To overcome these issues, researchers have turned to stable, lead-free alternatives such as halide double perovskites Cs_2AgBiX_6 (X = Cl, Br, I).[11–15]

Recently, Rani *et al.* studied new double antiperovskites, namely Na_6SOCl_2, Na_6SOBr_2, Na_6SOI_2, K_6SOCl_2, K_6SOBr_2, and

[a]*Department of Physics, Abbottabad University of Science and Technology, Abbottabad, KPK, Pakistan. E-mail: saeedy@alumni.kaust.edu.sa; yasirsaeedphy@aust.edu.pk; Tel: +(92)-3454041865*

[b]*Department of Physics, College of Science and Humanities, Prince Sattam Bin Abdulaziz University, P. O. Box 173, Al-Kharj 11942, Saudi Arabia*

[c]*Prince Sultan Bin Abdulaziz International Prize for Water Chair, Prince Sultan Institute for Environmental, Water and Desert Research, King Saud University, Riyadh, Saudi Arabia*

[d]*Department of Chemical and Biological Engineering, Gachon University, 1342 Seongnamdaero, Sujeong-gu, Seongnam-si 13120, Republic of Korea. E-mail: sohail.ahmed2015@gmail.com; Tel: +8201065596861*

K_6SOI_2, with bandgaps of 4.34 eV, 3.71 eV, 3.33 eV, 3.99 eV, 3.38 eV, and 2.90 eV, respectively, and showed that they are good candidates for thermoelectric applications.[16] Yu *et al.* predicted that Na_6SOI_2 is particularly promising for low-temperature solid-state sodium-ion battery applications.[17] Mebrouki *et al.* explained that the effect of temperature on the elastic constants C_{11}, C_{12}, and C_{44} of $BaVO_3$ becomes less significant as the temperature increases.[18] Djebari *et al.* determined parameters such as formation energy, tolerance factor, and octahedral factor to confirm the structural integrity of $A^{3+}B^{4+}(O_2N)^{7-}$ and $A^{2+}B^{5+}(O_2N)^{7-}$. Based on their calculated bandgaps, these compounds show potential for applications in ferroelectric and photovoltaic devices.[19] The thermal expansion coefficient has been reported to be adversely affected by changes in pressure and temperature.[20] Given that double antiperovskites have only recently been proposed, experimental and theoretical studies remain limited, highlighting opportunities for further investigation. Here, we are examining the double antiperovskites K_6NaAsX_2 (where X = Cl, Br, I) in terms of their structural, electrical, optical, mechanical, thermoelectric, photovoltaic, thermodynamic, and photocatalytic characteristics with a focus on materials exhibiting bandgaps comparable to that of MAPI.[21] We also compare our results with the previously studied double perovskite material $K_2NaAsCl_6$.[14]

2. Computational details

All simulations in this study are conducted using density functional theory (DFT), specifically the full-potential linearized augmented plane wave plus local orbitals (FP-LAPW + LO) method, which is renowned for its high accuracy in determining material properties. These computations were carried out using the WIEN2k code.[22] The Wu–Cohen generalized gradient approximation (WC–GGA) was employed to account for exchange–correlation effects, which are a crucial component of DFT.[23] The modified Becke–Johnson (mBJ) potential was applied on top of WC–GGA to improve the accuracy of bandgap predictions, addressing a well-recognized shortcoming of traditional DFT.[24,25] Lead halide perovskites are among the semiconductors for which this combination has previously been validated and shown to be in strong agreement with experimental data.[26–31] The majority of the calculations in this study were performed using a 13 × 13 × 13 *k*-point mesh. Thermoelectric and optical properties were evaluated more precisely with a denser 24 × 24 × 24 mesh. The BoltzTraP code was employed to calculate the thermoelectric properties of K_6NaAsX_2 (X = Cl, Br, I) over a temperature range of 300–900 K. The technical parameters included a kinetic energy cutoff of −7.0 Rydbergs to distinguish valence from core electrons. A plane-wave expansion cutoff of $G_{max} = 20$ and an angular momentum cutoff of $l_{max} = 12$ were used. Structural optimizations were performed until the total energy converged within 10^{-5} Ry,[32] ensuring highly accurate results.

3. Results and discussions

3.1 Structural properties

The first step in understanding a material's physical properties is a thorough examination of its structural features. This study focuses on optimizing the structural parameters of K_6NaAsX_2 (X = Cl, Br, I) by minimizing the total energy to obtain the ground-state configuration. Fig. 1(a) shows the crystal structure of K_6NaAsX_2, with initial lattice parameter taken from $K_2NaAsCl_6$ (10.31 Å) as a starting point. The energy–volume relationship, shown in Fig. 1(b), used for structural optimization. For fitting the nonlin- ear energy *vs.* volume curve, initial lattice parameters of Cs_2AgBiX_6 (X = Cl, Br) were also considered as reference points. The Birch–Murnaghan approach for the equation of state was used to derive the important structural parameters from this volume optimization, including the bulk modulus (*B* in GPa) and the lattice constant (a in Å).[33] The compounds' optimised lattice constants fall between 12.65 Å and 12.72 Å while the bulk moduli vary between 3.16 GPa and 4.19 GPa, as summarized in Table 1. Previously studied double perovskite compound $K_2NaAsCl_6$ has lattice parameter 10.31 Å.[14] In our study the lattice parameter of compound increases by making antiperovskite of $K_2NaAsCl_6$ compound.

For K_6NaAsX_2 (X = Cl, Br, I), the effective masses of electrons (m_e^*) and holes (m_h^*) are shown in Table 1. Since all of the values are less than silicon's electron effective mass ($m_e^* = 1.09$), these compounds appear to be ideal for high-performance device applications.[34]

The thermal stability of these double perovskites is confirmed by Table 1, which lists the calculated formation energies of the elements and compounds.[35] The Goldschmidt tolerance factor (τ_G) and the octahedral factor (μ) were also used to evaluate the stability of the double antiperovskite materials.[36]

The ionic radii of K, Na, As, Cl, Br, and I are 1.38 Å, 0.95 Å, 0.58 Å, 1.81 Å, 1.96 Å, and 2.20 Å, respectively. For perovskites and antiperovskites, the crystal structure stability ranges are

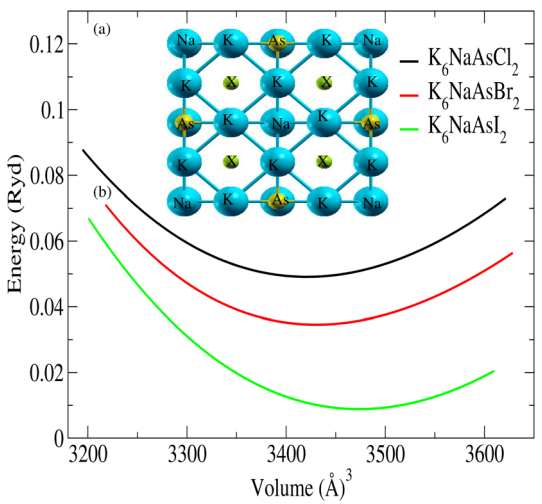

Fig. 1 For cubic double antiperovskites, (a) crystal structure and (b) the energy *vs.* volume curve, K_6NaAsX_2 (X = Cl, Br, I).

Table 1 Optimized lattice parameters a (Å), bulk modulus B (GPa) and Bandgap E_g (eV) of double antiperovskites Cs_6AgBiX_2 (X = Cl, Br, I) with SCF, SOC and hybrid, goldschmidt tolerance factor (τ_G), octahedral factor μ, formation energy E_f (eV), effective mass of electron (m_e^*) and effective mass of hole (m_h^*)

Materials	a	B	E^{GGA}	$E^{GGA+SOC}$	Hybrid	τ_G	μ	E_f	m_e^*	m_h^*
$K_6NaAsCl_2$	12.65	3.16	0.62	0.58	1.48	0.87	0.42	−2.06	0.32	0.40
$K_6NaAsBr_2$	12.66	4.06	0.61	0.57	1.34	0.91	0.39	−1.94	0.12	0.25
K_6NaAsI_2	12.72	4.19	0.60	0.54	1.16	0.85	0.34	−1.79	0.03	0.26
$K_2NaAsCl_6$	10.31 [14]	—	—	—	3.52 [14]	—	—	—	—	—

$0.415 < \mu < 0.895$ and $0.183 < \tau_G < 1.107$.[36] Table 1 shows that the calculated octahedral factor (μ) and Goldschmidt tolerance factor (τ_G) fall within these ranges, confirming the structural stability of all the compounds.

3.2 Electronic band structure

The electronic band structure is a crucial aspect of understanding a material's behavior, as it provides key insights into its metallic or semiconducting nature. It directly affects essential properties such as the optical response and electrical resistivity, which are critical for device design. The band structures of K_6NaAsX_2 (X = Cl, Br, I) were calculated to investigate their electronic characteristics. Initially, a self-consistent field (SCF) method was used to estimate the bandgaps. Spin–orbit coupling (SOC) and the modified Becke–Johnson (mBJ) potential were then applied to improve agreement with experimental trends and refine the bandgap values, particularly for compounds with gaps below 1 eV. As a validation step, we also recalculated the bandgap of $K_2NaAsCl_2$, previously reported to be 3.52 eV.[14] Our calculated bandgap values for K_6NaAsX_2 (X = Cl, Br, I) using the mBJ + SOC (hybrid) approach are 1.48 eV, 1.34 eV, and 1.16 eV, respectively (Fig. 3(a–c)). For comparison, the previously reported double perovskite $K_2NaAsCl_6$ has a bandgap of 3.52 eV,[14] indicating that our study provides improved bandgap predictions for antiperovskites. Without SOC, the bandgaps are 0.62 eV, 0.61 eV, and 0.60 eV, while with SOC they decrease slightly to 0.58 eV, 0.57 eV, and 0.54 eV, respectively. Furthermore, our goal was to obtain bandgap values close to the experimental observations for MAPI, which exhibits a direct bandgap at a high-symmetry point, a feature also reproduced in our studied compounds.[32] Our analysis indicates that the FP-LAPW + lo method, when used alone, significantly underestimates the bandgap values of double antiperovskites. Therefore, our goal is to obtain a bandgap close to 1.55 eV while using lead-free materials, making these compounds promising candidates to replace MAPI for room-temperature applications.[37]

The computed materials exhibit a direct bandgap both with and without SOC, as shown in Fig. 2(a–c). A slight decrease in bandgap values was observed for K_6NaAsX_2 (X = Cl, Br, I) upon SOC application. A bandgap close to 1.55 eV is ideal for efficient semiconductor photovoltaic devices, as it allows effective electron excitation with minimal heat loss. Although direct bandgaps are observed in several recently investigated double antiperovskites, their values often fall outside this ideal range. Conversely, compounds with suitable bandgaps are typically indirect, which limits their usefulness in solar applications. Pressure-induced bandgap tuning could be a practical strategy to bring the bandgap closer to the ideal 1.55 eV.

3.3 Density of states (DOS)

We investigated density of states (DOS) of K_6NaAsX_2 (X = Cl, Br, I), focusing on the atomic-level contributions. From Fig. 4(a–c) analysis reveals that potassium (K) and arsenic (As) atoms predominantly contributed to the Valence Band Maxima (VBM) in all three compounds, while the Conduction Band Minima (CBM) arises from a combination of K, Na, and halogen (Cl, Br, or I) states. Notably, K atoms play a significant role in determining the bandgap. A more detailed examination of the PDOS provides further insight, and Fig. 4 illustrates the distinct orbital contributions of X= Cl, Br in the VBM and CBM regions.

The K-p orbital predominates in the CBM, whereas the As-p orbital makes a substantial contribution to the VBM, as shown in Fig. 4(a). Contributions from other atoms are relatively minor. The Cl-p orbital also exhibits a notable presence in the CBM, while d-orbital contributions to the VBM are limited. Within the VBM, Cl's p-orbital exerts a stronger influence than those of Na and As, and K's d-orbital extends throughout the valence region down to −5 eV. In contrast, Br's d-orbital contributes negligibly to both the VBM and CBM. As shown in Fig. 4(b), a similar pattern emerges: the CBM is primarily influenced by the d-orbital of K and the p-orbital of Br, while the VBM is mainly governed by the p-orbital of K. In Fig. 4(c), the CBM is largely shaped by the p-orbitals of both I and K, whereas the VBM shows a dominant contribution from the d-orbital of K. These recurring orbital characteristics underscore the significant roles of halogen p-orbitals and potassium orbitals in shaping the electronic structure of K_6NaAsX_2 (X = Cl, Br, I).

3.4 Optical properties

The advancement of optical technologies depend on the optical properties of materials. Perovskites have become one of the most optimistic materials for high-efficiency optoelectronic applications.[37,38] A material's interaction with an external electromagnetic field is described by its complex dielectric function, which is $\epsilon(\omega) = \epsilon_1(\omega) + i\epsilon_2(\omega)$.[39] In this expression, $\epsilon_1(\omega)$ symbolizes the real component, which has to do with the material's dispersion, while $\epsilon_2(\omega)$ is the imaginary part, which accounts for absorption.

$\epsilon_1(\omega)$, represents the dielectric constant and indicates a material becomes polarized in electric field due to induced

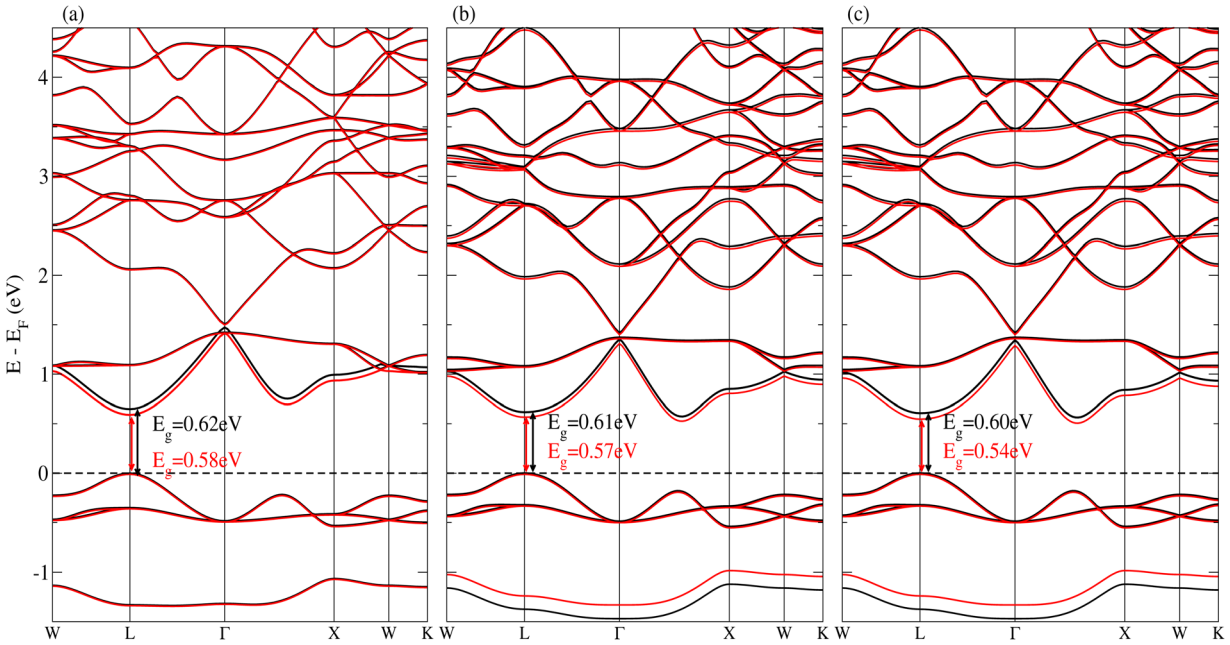

Fig. 2 The band structures of (a) $K_6NaAsCl_2$ (b) $K_6NaAsBr_2$, and (c) K_6NaAsI_2 without SOC (black) and with SOC (red).

dipole formation. The imaginary part, $\in_2(\omega)$, reflects the material's ability to absorb and attenuate electromagnetic radiation. These dielectric properties are closely linked to the material's electronic structure, particularly through the momentum transition matrix elements and the joint density of states (DOS). Furthermore, $\in_1(\omega)$ can be obtained from $\in_2(\omega)$ using the Kramers–Kronig relations.[40] When $\in_1(\omega) > 0$, light can propagate through the material; when $\in_1(\omega) < 0$, the electromagnetic wave is attenuated and cannot propagate.[41,42]

The frequency-dependent real and imaginary components of the dielectric function provide important information about the optical characteristics of a material, such as its refractive index, absorption coefficient, reflectivity, and optical conductivity. The refractive index, $n(\omega)$, and the extinction coefficient, $k(\omega)$, are the two main factors that define the optical response.[43,44]

$$\begin{cases} n(\omega)^2 - k(\omega)^2 = \varepsilon_1(\omega) \\ 2n(\omega)k(\omega) = \varepsilon_2(\omega) \end{cases}$$

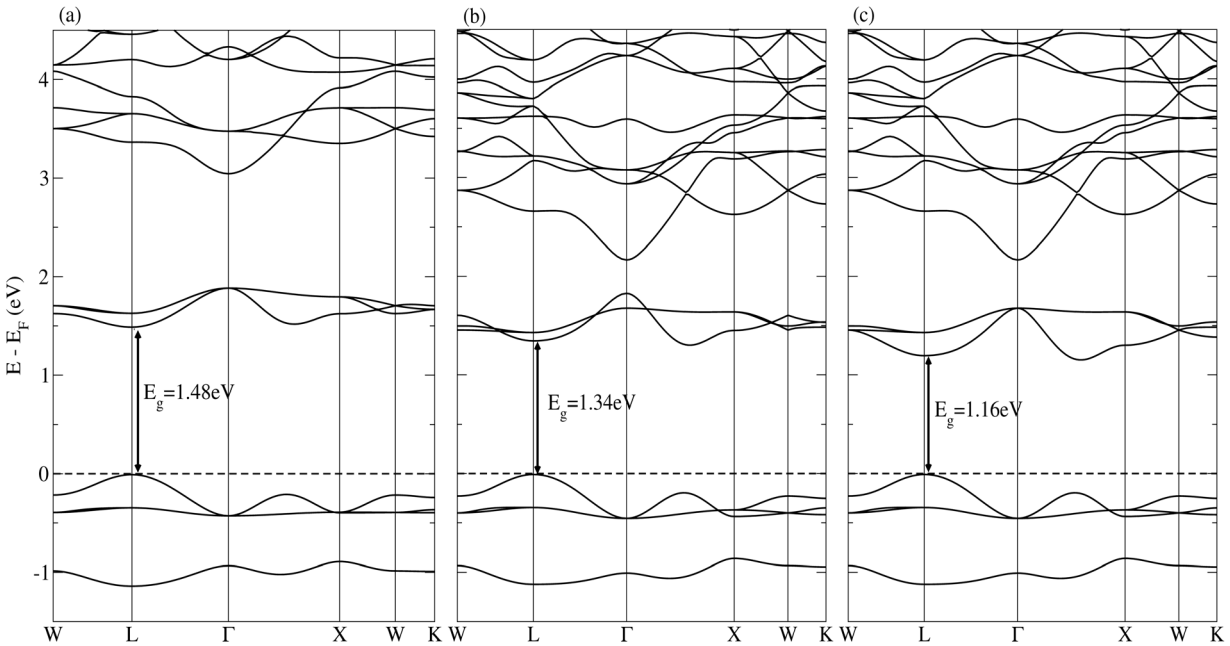

Fig. 3 The band structures of (a) $K_6NaAsCl_2$ (b) $K_6NaAsBr_2$, and (c) K_6NaAsI_2 with hybrid.

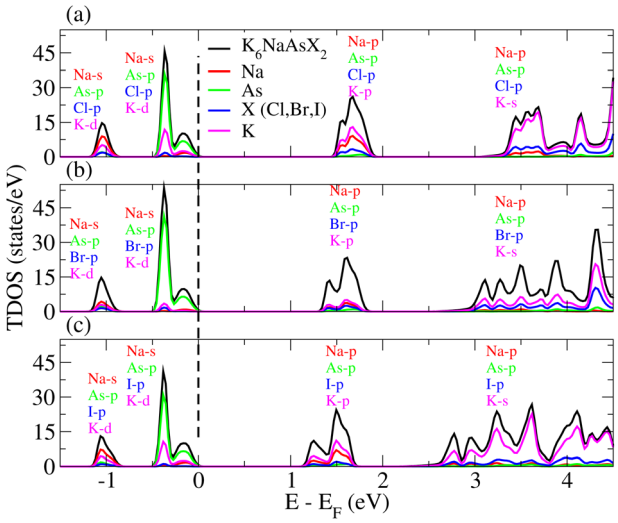

Fig. 4 Density of States(DOS) of (a) $K_6NaAsCl_2$, (b) $K_6NaAsBr_2$ (c) K_6NaAsI_2.

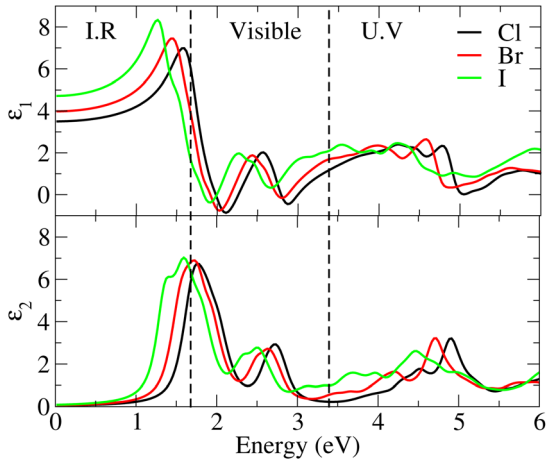

Fig. 5 Optical properties of K_6NaAsX_2 (X = Cl, Br, I).

where $n(\omega)$ governing phase velocity and $k(\omega)$ give information about absorption of material.

The compounds K_6NaAsX_2 (X = Cl, Br, I) exhibit high static dielectric constants, $\in_1(\omega)$, of 6.94, 7.43, and 8.34, respectively. These values are substantially higher than those of other potential solar cell materials, including $MAPbI_3$ (5.4), $FAPbI_3$ (5.7), $Cs_2LiTlBr_6$ (1.6), $Cs_2NaTlBr_6$ (1.7), and Cs_2AgCrI_6 (5.7).[40,45–49] Materials with a high dielectric constant are beneficial for solar cell applications, as their enhanced polarization and reduced exciton binding energies facilitate more efficient charge separation and transport.[50,51] For the chloride, bromide, and iodide-based compounds, the real part of the dielectric function, $\in_1(\omega)$, shows maximum polarization values of 2.01, 1.83, and 1.94 inside the visible range at photon energies of 2.50 eV, 2.45 eV, and 2.28 eV, respectively. At photon energies of 1.78 eV, 1.73 eV, and 1.59 eV, respectively, the imaginary part of the dielectric function, $\in_2(\omega)$, representing optical absorption, peaks at 6.71, 6.81, and 7.02 for the chloride, bromide, and iodide compounds. These values are marginally outside the visible range. The first peak at 1.5 eV originates from direct transitions at the band edge, where halogen p-derived valence states transition to the conduction-band minimum dominated by Na-site cation s orbitals. The second peak around 2.6 eV is mainly attributed to transitions from deeper halogen p states and K-site hybridized orbitals in the valence band to conduction states. The higher-energy feature at 4.8 eV is associated with transitions from lower valence states to high-lying conduction bands with strong As d character, consistent with the large joint density of states in this region[52,53] These results, shown in Fig. 5, demonstrate the materials' linear optical response. We also calculated key optical properties, including the optical conductivity, $\sigma(\omega)$, reflectivity, $R(\omega)$, extinction coefficient, $k(\omega)$, absorption coefficient, $\alpha(\omega)$, and refractive index, $n(\omega)$, to further evaluate their optoelectronic behavior, as illustrated in Fig. 6. The static dielectric constants, $\in(0)$, for $K_6NaAsCl_2$, $K_6NaAsBr_2$, and K_6NaAsI_2 are 2.97, 2.99, and 3.20, respectively,[35] aligned well with our observations.

As shown in Fig. 6(a), the static refractive indices, $n(\omega)$, for $K_6NaAsCl_2$, $K_6NaAsBr_2$, and K_6NaAsI_2 are 3.11, 3.13, and 3.14, respectively. The maximum values of $n(\omega)$ and the extinction coefficient, $k(\omega)$, occur at photon energies of 1.64 eV and 2.01 eV for $K_6NaAsCl_2$, 1.51 eV and 1.83 eV for $K_6NaAsBr_2$, and 1.29 eV and 1.67 eV for K_6NaAsI_2. As shown in Fig. 6(b), the optical conductivity, $\sigma(\omega)$, for $K_6NaAsCl_2$ reaches a maximum value of 2.17×10^4 $(\Omega\ cm)^{-1}$ at 2.74 eV, while $K_6NaAsBr_2$ and K_6NaAsI_2 peak at 1.91×10^4 $(\Omega\ cm)^{-1}$ at 2.66 eV and 1.87×10^4 $(\Omega\ cm)^{-1}$ at 2.54 eV, respectively. This indicates that $K_6NaAsCl_2$ exhibits the highest optical conductivity within the visible light range (1.87–2.17 eV), which is beneficial for photovoltaic applications. The absorption coefficient has a direct correlation with solar energy conversion efficiency, which quantifies how far specific light frequencies penetrate the material before being absorbed. As shown in Fig. 6(c), the absorption coefficient, $\alpha(\omega)$, exhibits peak values of 3.2×10^5 cm^{-1} at 2.86 eV (433.51 nm) for $K_6NaAsCl_2$, 2.85×10^5 cm^{-1} at 2.73 eV for $K_6NaAsBr_2$, and 2.60×10^5 cm^{-1} at 1.84 eV for K_6NaAsI_2. These results are comparable to MAPI, which exhibits absorption in the range of 10^4–10^5 cm^{-1}, indicating strong absorption in the visible region, particularly for $K_6NaAsCl_2$. As illustrated in Fig. 6(d), the maximum reflectivity, $R(\omega)$, for $K_6NaAsCl_2$, $K_6NaAsBr_2$, and K_6NaAsI_2 is 0.32%, 0.31%, and 0.30% at approximately 0.21 eV, 0.19 eV, and 1.86 eV, respectively. These low reflectivity values suggest efficient light absorption, which is beneficial for photovoltaic performance.

3.5 Photocatalytic properties

Direct bandgap semiconductor materials can effectively harness solar energy for hydrogen production through water splitting.[54,55] This process offers a promising route for generating clean, renewable energy *via* photocatalytic water splitting.[56,57] In this process, photo-generated holes oxidize water molecules, while the excited electrons drive the corresponding reduction reaction.[58]

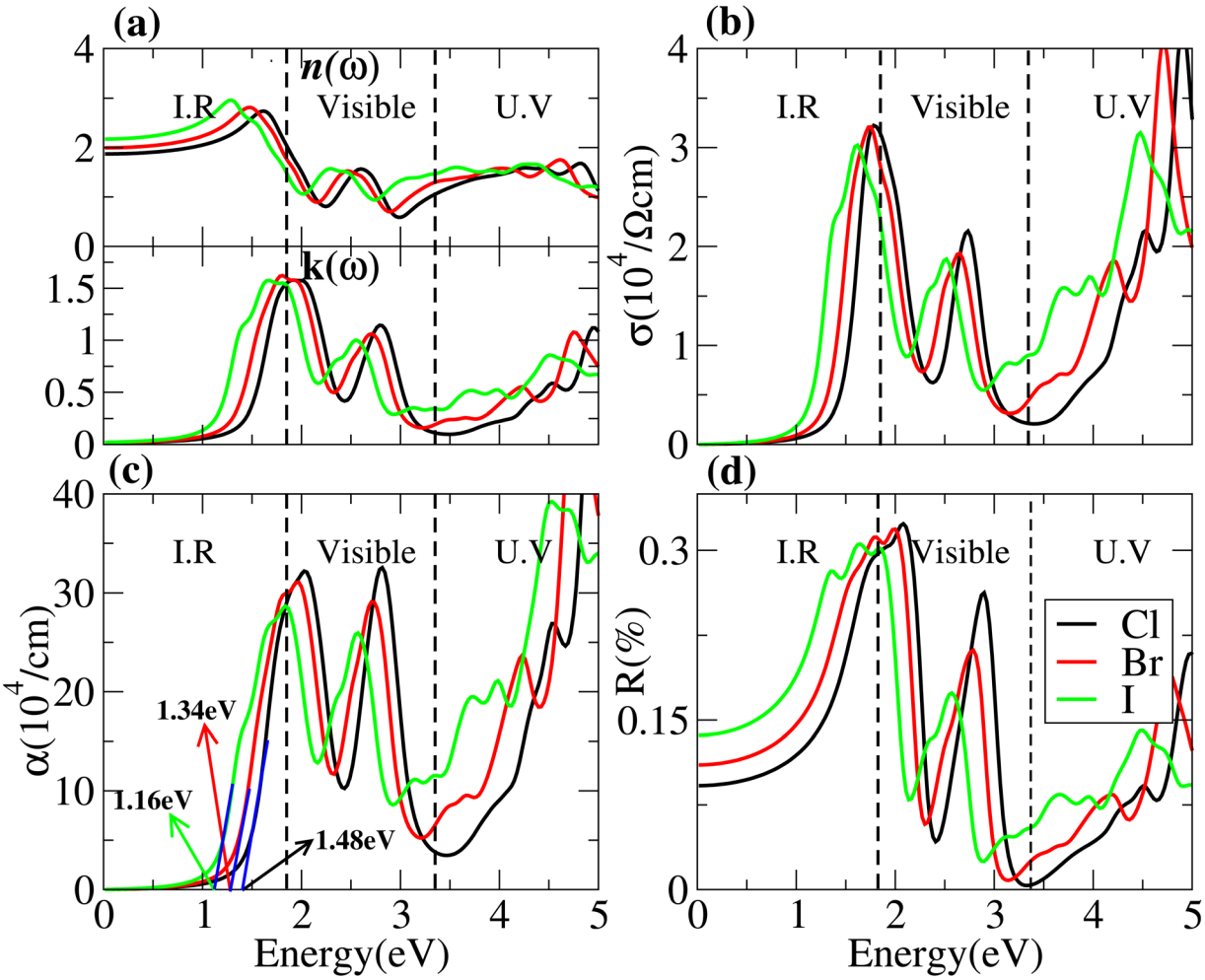

Fig. 6 Optical properties (a) refracrive index, (n, k), (b) optical conductivity, σ, (c) absorption coefficient, α and (d) reflectivity, R of K_6NaAsX_2 (X = Cl, Br, I).

A material must have a valence band maximum (VBM) below the O_2 oxidation potential (1.23 eV) and a conduction band minimum (CBM) above the H^+ reduction potential (0 eV) in order to be appropriate for photocatalytic water splitting. This alignment ensures that photo-generated holes can drive water oxidation, while excited electrons facilitate proton reduction. To assess this criterion, Mulliken electronegativity is used to estimate the locations of the valence and conduction band edges in the studied materials (Table 2).[59]

Fig. 7 illustrates that, in photocatalytic water splitting, the redox potentials are referenced against the standard hydrogen electrode (SHE) and then converted to the vacuum energy scale, which is commonly used in solid-state physics. These values indicate the energy levels at which electrons must be supplied (for reduction) or removed (for oxidation) for the redox reactions to proceed. To enable water splitting under sunlight, a material's CBM must be 0 eV, allowing electrons to reduce H^+, while its VBM must be 1.23 eV to accept electrons from water and drive oxygen evolution.[60] This reference allows the CBM and VBM of the material to be positioned relative to the water redox potentials.[61] The conduction band (CB) and valence band (VB) potentials of a photocatalyst shift with pH, typically by about 0.059 eV per pH unit as calculated by using Nernst equation. At lower pH = 0, the CB and VB potentials are more positive, making the holes more oxidative but potentially reducing the efficiency of electron-driven reductions. When pH increases from 0 to 7 the band edges increase. At pH = 7, the band edges are less positive, which may favor reduction reactions but could weaken the oxidative power of holes for certain reactions.[62]

Table 2 Photocatalytic parameters of K_6NaAsX_2 (X = Cl, Br, I) at pH = 0

Compounds	χ (eV)	E_g (eV)	E_{CB} (eV)	E_{CB} (eV)
$K_6NaAsCl_2$	1.09	1.48	2.66	1.18
$K_6NaAsBr_2$	1.08	1.34	2.74	1.40
K_6NaAsI_2	1.07	1.16	2.85	1.69

From the figure, it is evident that all studied materials possess suitable VBM positions for water oxidation, but their CBM positions lie below the required level for water reduction, indicating that they are ineffective for complete water splitting

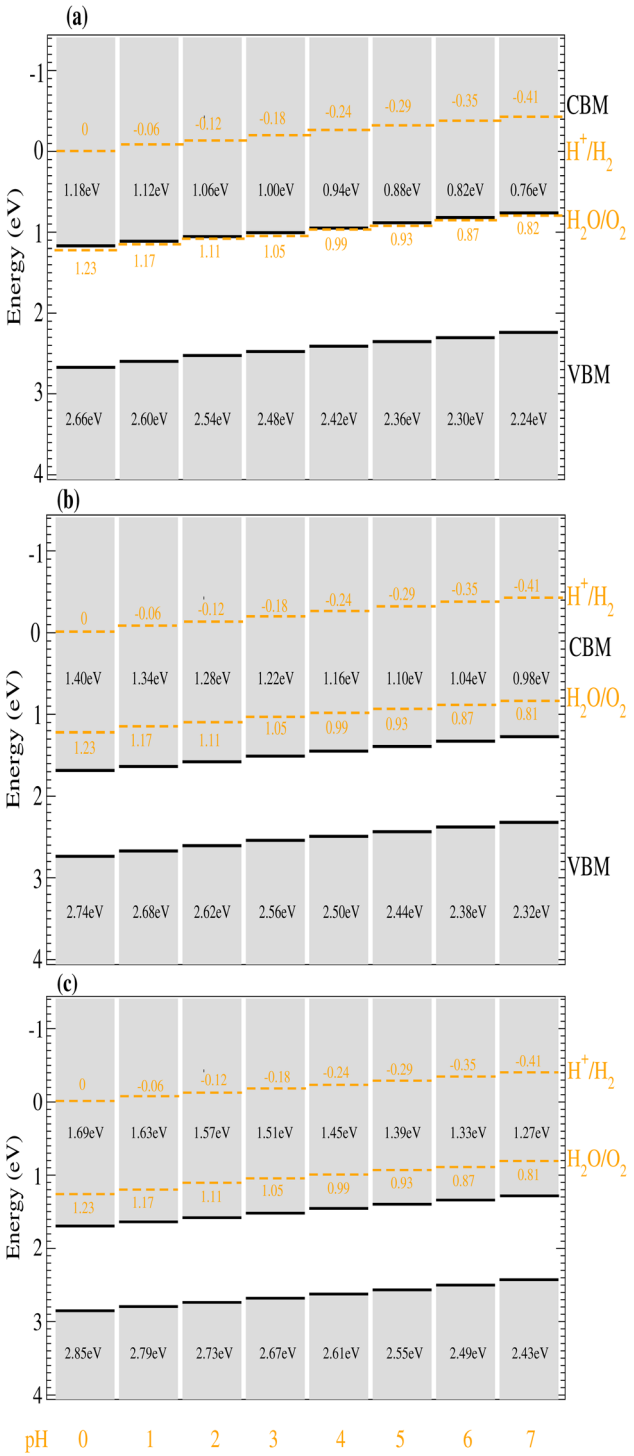

Fig. 7 Photo-catalytic properties of (a) $K_6NaAsCl_2$ (b) $K_6NaAsBr_2$, and (c) K_6NaAsI_2.

via photocatalysis. The band-edge alignment of the three double antiperovskite compounds, K_6NaAsX_2 (X = Cl, Br, I), show good response for oxidation relative to the water-splitting redox potentials across different pH values.[63,64]

3.6 Thermoelectric properties

In metallic compounds, the high density of free electrons tends to cancel out potential differences, leading to low Seebeck coefficient values. Since electrons in metals transport both charge and heat, thermal energy can flow easily through the material. This high thermal conductivity is undesirable for thermoelectric applications, as it diminishes the temperature gradient required for efficient power generation. Overall, the combination of a low Seebeck coefficient(S) and high electronic thermal conductivity (κ_e) makes metals inefficient for thermoelectric (TE) applications. In insulators, the low carrier concentration allows even a small temperature difference to generate a large voltage, resulting in a high Seebeck coefficient (hundreds to thousands of $\mu V\ K^{-1}$). Since there are very few free electrons, heat is not efficiently conducted electronically, which is beneficial for thermoelectric efficiency. However, the lack of mobile charge carriers limits power generation. Optimal thermoelectric materials achieve a balance between electrical conductivity and thermal insulation. Materials with an electronic carrier concentration on the order of 10^{19} cm^{-3} are considered ideal for efficient thermoelectric performance.[65]

Fig. 8(a) illustrates the temperature dependence of the Seebeck coefficient, S ($\mu V\ K^{-1}$). As shown in Table 3, the peak value of S at 300 K is observed for K_6NaAsI_2, reaching 250.19 $\mu V\ K^{-1}$, while $K_6NaAsBr_2$ exhibits the lowest value at 204.53 $\mu V\ K^{-1}$. The Seebeck coefficient of $K_6NaAsCl_2$ lies between the other two materials, at 240.13 $\mu V\ K^{-1}$ at 300 K, which is significantly higher than that of the previously reported double perovskite $K_2NaAsCl_6$ (199 $\mu V\ K^{-1}$ at 300 K).[14] Across all three compounds, the decrease in Seebeck coefficient with increasing temperature while remaining positive. At 900 K, $K_6NaAsCl_2$ exhibits the lowest Seebeck coefficient among the studied materials.

The electrical conductivity's temperature dependency, represented as σ/τ ($1\ \Omega^{-1}\ ms^{-1}$), is displayed in Fig. 8(b). At room temperature (300 K), the highest σ/τ value is observed for $K_6NaAsCl_2$, reaching 4.65×10^{18} ($1\ \Omega^{-1}\ ms^{-1}$), while the lowest is recorded for K_6NaAsI_2 at 2.70×10^{18} ($1\ \Omega^{-1}\ ms^{-1}$). For the previously reported double perovskite $K_2NaAsCl_6$, this value reaches 4.31×10^{18} ($1\ \Omega^{-1}\ ms^{-1}$).[14] For all compounds, electrical conductivity increases with rising temperature. At 900 K, $K_6NaAsBr_2$ exhibits the highest σ/τ value of 11.82×10^{18} ($1\ \Omega^{-1}\ ms^{-1}$), whereas $K_6NaAsCl_2$ shows a lower value of 10.14×10^{18} ($1\ \Omega^{-1}\ ms^{-1}$). First-principles electron–phonon coupling would provide a more quantitative description, which we identify as a direction for future work.

Fig. 8(c) demonstrates how the electronic contribution to thermal conductivity varies with temperature, denoted as κ_e/τ (in units of 10^{14} $W\ mK^{-1}\ s^{-1}$). The contribution of charge carriers, such as electrons or holes, to the overall thermal conductivity is represented by this number. The Wiedemann–Franz law ($\kappa = L \times \sigma \times T$), where L is the Lorentz number, σ is the electrical conductivity, and T is the absolute temperature, establishes a direct relationship between the electrical conductivity (σ) and the electronic thermal conductivity (κ_e). Since both κ_e/τ and σ/τ are proportional to each other (sharing the same relaxation time, τ), they exhibit similar trends with

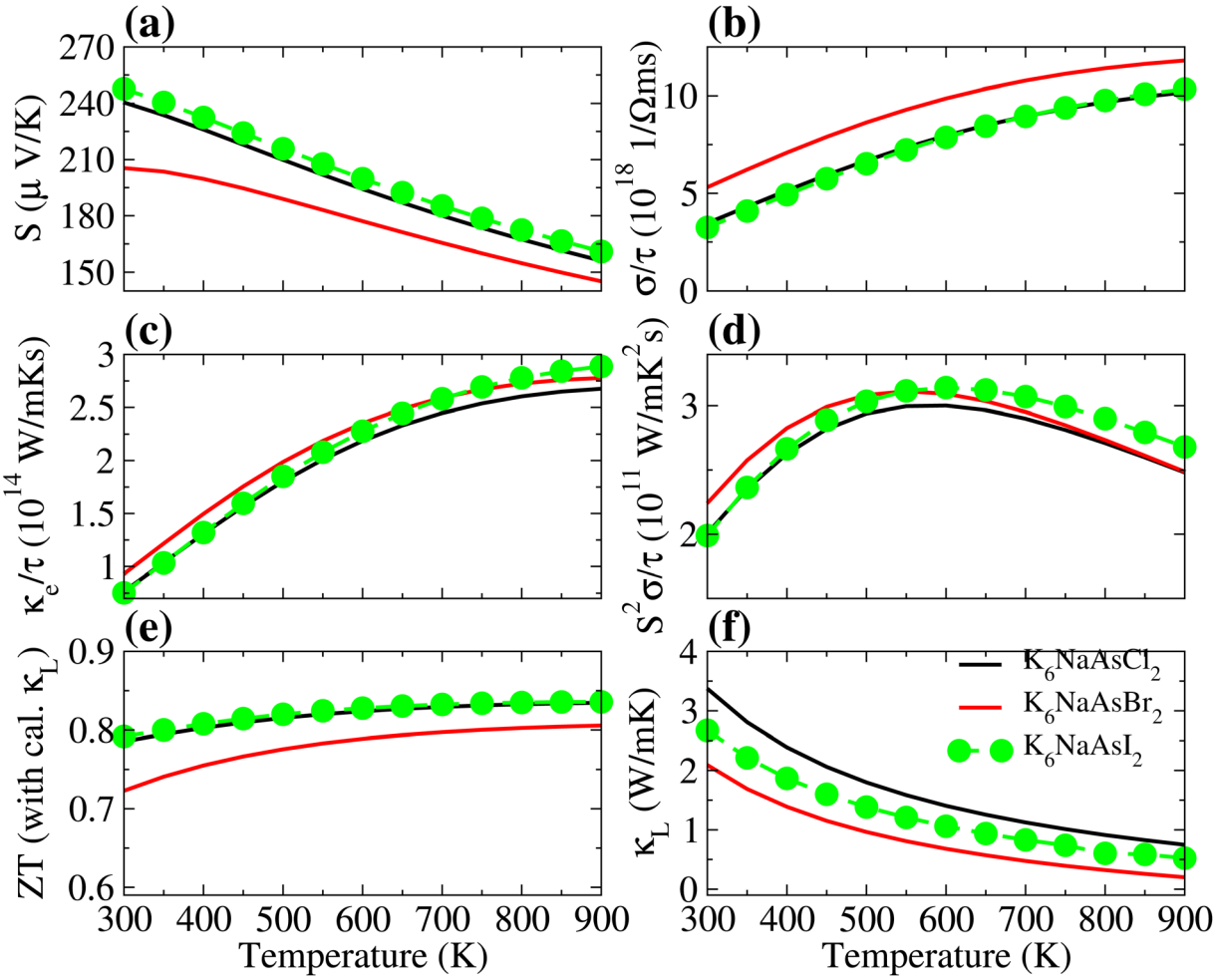

Fig. 8 Thermoelctric properties (a) seebeck coefficient, S, (b) electronic conductivity, σ/τ , (c) electronic thermal conductivity, κ_e/τ, (d) power factor, $S^2\sigma/\tau$, (e) figure of merit, ZT, and (f) lattice thermal conductivity, κ_L, with temperature variation from 300 K to 900 K for K_6NaAsX_2 (X = Cl, Br, I).

Table 3 Thermoelectric propertes, S (μV K^{-1}), $\sigma/\tau(10^{18} \times 1\ \Omega^{-1}\ ms^{-1})$, $\kappa_e/\tau(10^{14} \times W\ mK^{-1}\ s^{-1})$, κ_L(W mK^{-1}), PF(10^{11} W $mK^{-2}\ s^{-1}$) and ZT (1 K^{-1}) (with calcuated κ_L at 300 K for K_6NaAsX_2 (X = Br, Cl)

Compounds	S	σ/τ	κ_e/τ	κ_L	PF	ZT@κ_L
$K_6NaAsCl_2$	240.13	4.65	0.59	3.34	1.99	0.77
$K_6NaAsBr_2$	204.53	2.88	0.74	2.03	2.24	0.71
K_6NaAsI_2	250.19	2.70	0.57	2.60	1.98	0.78
$K_2NaAsCl_6$	199[14]	4.31 [14]	0.36 [14]	—	1.72 [14]	0.11 [14]

temperature. Consequently, the κ_e/τ curve closely mirrors the behavior observed for σ/τ.

At 300 K, the lowest κ_e/τ is estimated for K_6NaAsI_2 at 0.57 × 10^{14} W mK^{-1} s^{-1}, whereas $K_6NaAsBr_2$ exhibits the highest value of 0.74 × 10^{14} W mK^{-1} s^{-1} at the same temperature. For the previously reported double perovskite $K_2NaAsCl_6$, this value is 0.36 × 10^{14} W mK^{-1} s^{-1},[14] which increases to 0.59 × 10^{14} W mK^{-1} s^{-1} in the antiperovskite $K_6NaAsCl_2$. A similar trend is consistently observed across the entire temperature range, remaining stable even at elevated temperatures up to 900 K.

Fig. 8(d) illustrates the temperature dependence of the electronic power factor (PF), expressed in units of W mK^{-2} s^{-1}. The power factor is calculated using the relation: PF = $S^2 \times \sigma/\tau$; at room temperature (300 K), the maximum PF is predicted for $K_6NaAsBr_2$, reaching 2.40 × 10^{11} W mK^{-2} s^{-1}, whereas the lowest value of 1.98 × 10^{11} W mK^{-2} s^{-1} is observed for K_6NaAsI_2. The PF for $K_6NaAsCl_2$ is 1.99 × 10^{11} W mK^{-2} s^{-1}, which is higher than that of the previously reported double perovskite $K_2NaAsCl_6$ (1.99 × 10^{11} W mK^{-2} s^{-1}).[14] A similar trend is maintained at higher temperatures.

For most solid materials, thermal conductivity generally decreases with increasing temperature. Slack's equation offers a thorough understanding of heat transfer in solids and is frequently used to determine the temperature-dependent lattice thermal conductivity.[66,67]

The lattice thermal conductivity, κ_L (W mK^{-1}), calculated using Slack's method, is shown in Fig. 8(f). Increased phonon scattering, thermal expansion, and weakening of interatomic bonds are the causes of the observed reduction in κ_L with increasing temperature. At 300 K, $K_6NaAsCl_2$ exhibits the

highest lattice thermal conductivity of 3.34 W mK^{-1}, whereas $K_6NaAsBr_2$ shows the lowest value of 2.03 W mK^{-1}. The lower κ_L in $K_6NaAsBr_2$ contributes to its highest thermoelectric figure of merit (ZT) at 450 K (see Fig. 8(e)). Increased phonon–phonon scattering, which hinders the passage of thermal energy and lowers lattice thermal conductivity, results from lattice vibrations (phonons) being more energetic and exhibiting increasing frequency dependence as temperature rises. Interatomic lengths are further changed by thermal expansion, which has an impact on thermal transport and phonon dispersion.[68,69] Additionally, elevated temperatures can weaken interatomic bonding, decreasing phonon group velocities and further lowering κ_L. Understanding these factors provides a comprehensive explanation for the temperature-dependent decline in lattice thermal conductivity.

A dimensionless metric known as the figure of merit, or ZT, is used to quantify a thermoelectric material's performance or efficiency, which is its capacity to transform heat into electricity. ZT is inversely proportional to total thermal conductivity ($\kappa = \kappa_e + \kappa_L$) and directly proportional to power factor (PF). The goal is to decrease thermal conductivity and maximize power factor (high Seebeck coefficient and electrical conductivity) in order to raise ZT. ($ZT = S^2\sigma/\kappa_e + \kappa_L$). As shown in Fig. 4(e), the ZT values at 300 K, calculated using the average total thermal conductivity (κ), which includes both electronic and lattice contributions, range from 0.71 to 0.78. Among the studied compounds, K_6NaAsI_2 exhibits the highest ZT value of 0.78 at 300 K, primarily due to its comparatively lower lattice thermal conductivity (κ_L). The ZT value for $K_6NaAsCl_2$ is reported as 0.77, which is much greater than that of the adjacent perovskite $K_2NaAsCl_6$, which has a value of 0.11.[14]

3.7 Thermodynamic properties

One of the key thermodynamic parameters frequently analyzed in materials is the heat capacity (C_P). Although it is one of the more challenging quantities to interpret physically, it provides significant insight, with over six distinct definitions available.[70] Fig. 9(a) shows that the heat capacity at constant pressure (C_P) increases rapidly at low temperatures and then begins to plateau. Among the three compounds, K_6NaAsI_2 (green) exhibits the highest C_P, followed by $K_6NaAsBr_2$ (red), and then $K_6NaAsCl_2$ (black). This trend likely reflects the increasing atomic mass of the halides (Cl < Br < I), which affects vibrational modes and, consequently, the heat capacity. The heat capacity at constant volume (C_V) can provide additional information regarding solid-phase transitions, energy band structure, and lattice vibrations.[71]

The results for the heat capacity at constant volume (C_V) are presented in Fig. 9(b). C_V increases quickly below 300 K, while the rate of increase slows down at higher temperatures. In accordance with the Dulong–Petit limit, C_V approaches a constant value at 1000 K, reaching a maximum of 247 cal per cell per K. At any given temperature, C_V increases in the order of Cl < Br < I, reflecting the influence of the halide atomic mass on lattice vibrations. Understanding a material's thermal behavior is essential, as energy conversion and heat dissipation occur

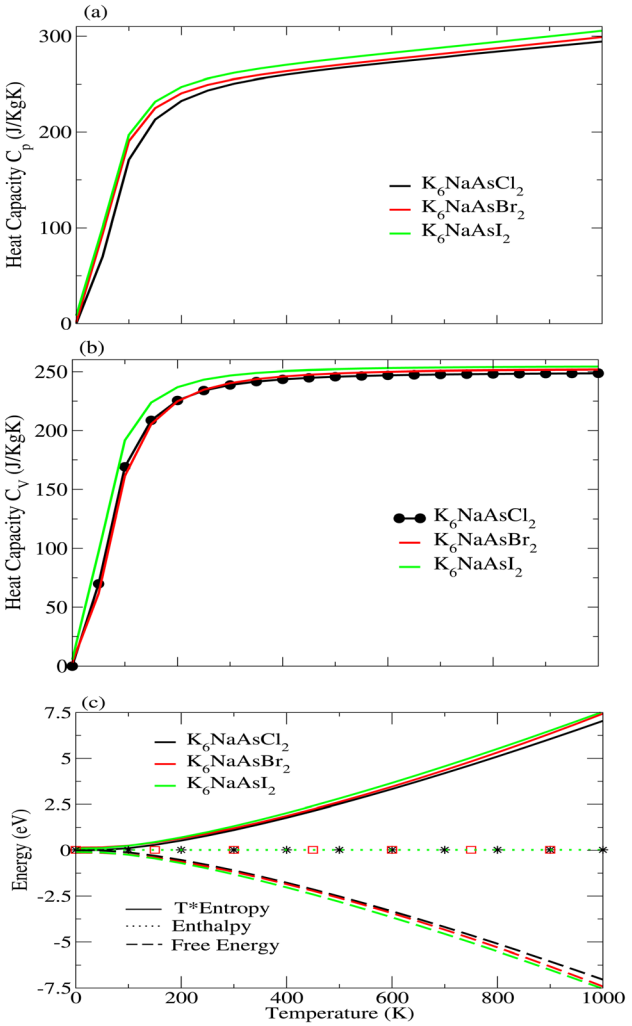

Fig. 9 Thermodynamic properties (a) heat capacity, C_p, (b) heat capacity, C_v, and (c) energies, with temperature variation from 0 K to 1000 K for K_6NaAsX_2 (X = Cl, Br, I).

during practical use. Fig. 9(c) shows the temperature-dependent variations of entropy multiplied by temperature (TS), enthalpy (H), and Gibbs free energy (F), represented by the top, middle, and bottom curves, respectively. These quantities provide insight into the thermodynamic stability and energy characteristics of the compounds. The formulas are $H = U + pV$ and $F = U - TS$, where U, p, and V represent the internal energy, pressure, and volume of the system, respectively. The $T{\cdot}S$ curves become steeper as C_V gradually increases from Cl to Br and I at a constant temperature. Additionally, Fig. 9(c) shows that enthalpy (H) rises with temperature, $T{\cdot}S$ increases more rapidly, and Gibbs free energy (F) decreases, indicating enhanced thermodynamic stability at higher temperatures. Among the studied compounds, K_6NaAsI_2 (green) consistently exhibits the highest $T{\cdot}S$ and enthalpy values, along with the most negative free energy, suggesting superior thermal stability. Enthalpy rises as a result of the system's thermal motion being intensified by temperature increases, which also raise internal energy, pressure, and volume. $F = U - TS < U + pV - TS = H - TS$, $F < H$

$-TS < 0$ (ref. 71) since $H < TS$ and the three materials' enhanced range of H is less than TS.

3.8 SLME analysis

The spectroscopic limited maximum efficiency (SLME) approach was used to assess the photovoltaic efficiency of K_6NaAsX_2 (X = Cl, Br, I). The SLME method provides a more accurate estimate of the maximum power conversion efficiency of solar cells by extending the traditional Shockley–Queisser model by taking into account the material's thickness and absorption spectrum.[72]

The global sun spectrum (AM 1.5G), the absorption spectrum calculated from DFT calculations, and the fundamental and direct-allowed band gap (E_g) of the material are the input parameters used to calculate the SLME.[73] Fig. 10 presents the calculated SLME (%) for K_6NaAsX_2 (X = Cl, Br, I) at fixed thicknesses and temperatures. The results indicate that device temperature, band gap, and material thickness have the most significant impact on SLME. As shown in Fig. 10, SLME increases gradually with increasing material thickness and eventually saturates, approaching a constant value. In comparison K_6NaAsX_2 (X = Cl, Br, I) SLME efficiencies of @6.82%, @7.34% and @7.73% respectively for 0.5 μm thick layer, according to standard SLME analysis. Because of this, K_6NaAsI_2 is a better photovoltaic material and a compound that may be used in solar cell applications with a layer of material that is 500 nm thick. However, K_6NaAsX_2 (where X = Cl, Br, I) has maximum efficiency of @31.04%, @31.61%, and @32.41%. The experimental efficiency limit of $CH_3NH_3PbI_3$ is 25% for thicknesses of 0.4 and 0.5 μm.[74] The SLME approach shows that these compounds have a maximum effectiveness of more than 25%, proving the veracity of our findings.

3.9 Elastic properties

Because they show how a material reacts to external loads, effective elastic constants are crucial for evaluating a material's mechanical stability and practicality. Together with the bulk modulus (B) and shear modulus (G), the elastic constants C_{11}, C_{12}, and C_{44} determine a material's resistance to compression and deformation. When taking into account industrial applications, these factors are very crucial. The computed elastic constants for K_6NaAsX_2 (X = Cl, Br, I) are summarized in Table 4. For cubic crystals, the Born–Huang stability criteria must be satisfied: $C_{11} > 0$, $C_{44} > 0$, $C_{11} + 2C_{12} > 0$, $C_{11} - C_{12} > 0$, and $C_{12} < B < C_{11}$.[75] All studied materials meet these conditions, confirming their mechanical stability.

Table 4 Elastic properties of K_6NaAsX_2 (X = Cl, Br, I)

Compounds	$K_6NaAsCl_2$	$K_6NaAsBr_2$	K_6NaAsI_2
C_{11}	16.79	13.83	17.03
C_{12}	1.38	2.19	1.67
C_{44}	1.57	3.32	2.66
B	6.52	6.55	6.82
G_V	4.02	4.18	4.67
G_R	2.30	3.94	3.60
G	3.16	4.06	4.14
Y	10.02	10.33	11.40
B/G	2.06	1.61	1.64
C'	7.70	5.45	7.68
C''	−0.18	−0.41	−0.99
ν	0.27	0.23	0.22
A	0.20	0.60	0.34
A_z	1.27	1.69	1.41
A_u	3.73	0.30	1.47
ξ	0.23	0.36	0.25

The elastic constants of the materials can be further evaluated using the Voigt–Reuss–Hill (VRH) approximation, which offers a reliable approach to estimate macroscopic elastic moduli from elastic constants of the single crystal.[76,77]

In the Voigt–Reuss–Hill (VRH) approximation, the subscripts V and R refer to the Voigt and Reuss bounds, representing the upper and lower limits of the elastic moduli,

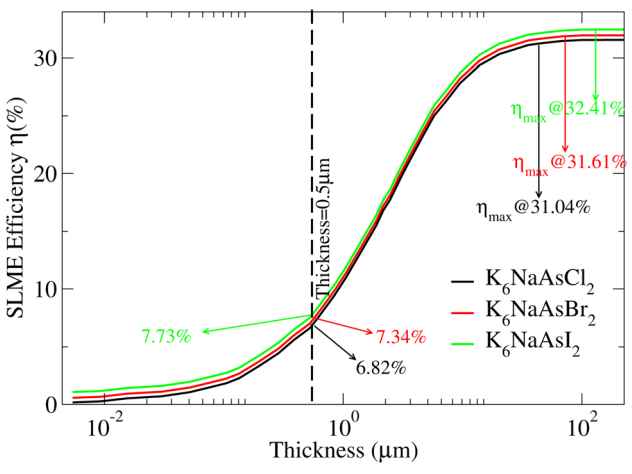

Fig. 10 SLME Efficiency (η) *vs.* Thickness (μm) of K_6NaAsX_2 (X = Cl, Br, I).

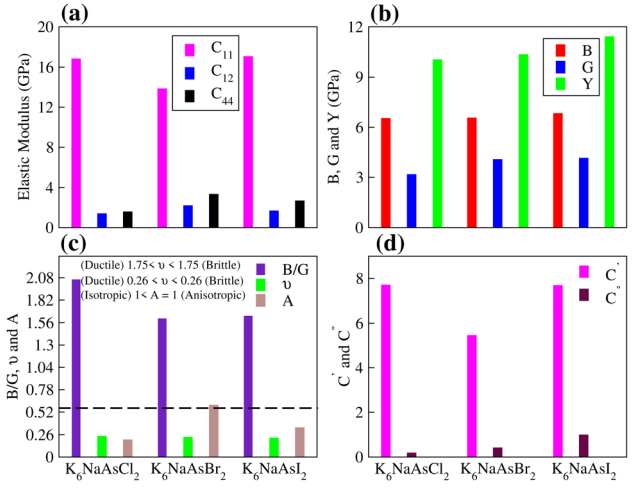

Fig. 11 Elastic properties (a) elastic modulus, (b) modulus (bulk B, shear G and young Y), (c) ratio's (Pugh's (B/G), Poisson's (ν) and isotropy index (A), and (d) cauchy's pressure values (C', C'') of K_6NaAsX_2 (X = Cl, Br, I).

respectively. As listed in Table 4, the Voigt shear moduli (G_V) for K_6NaAsX_2 (X = Cl, Br, I) are 4.02 GPa, 4.18 GPa, and 4.67 GPa, respectively. These values reflect the materials' resistance to shear deformation, indicating that they are relatively soft yet mechanically stable.

Poisson's ratio (μ) and Pugh's ratio (B/G) are widely used to evaluate a material's ductility and brittleness. A material is considered ductile if $\mu > 0.26$ or $B/G > 1.75$, whereas values below these thresholds indicate brittleness.[78] According to these criteria, $K_6NaAsBr_2$ and K_6NaAsI_2 are ductile, while $K_6NaAsCl_2$ is classified as brittle. Generally, ionic materials have μ values ranging from 0.3 to 0.4, with the theoretical upper limit being 0.5, whereas covalent materials typically exhibit lower μ values around 0.2. For K_6NaAsX_2 (X = Cl, Br, I), the calculated Poisson's ratios are 0.27, 0.23, and 0.22, respectively, suggesting that these compounds exhibit more covalent than ionic character (Fig. 11).[79]

Elastic anisotropy is closely associated with the formation of microcracks under mechanical stress, which can impact the durability and reliability of materials in practical applications. To evaluate this property, the elastic anisotropy index was calculated for K_6NaAsX_2 (X = Cl, Br, I).[80]

A material is considered isotropic if the anisotropy index A equals 0 or 1; any deviation from these values indicates elastic anisotropy.[80,81] The mechanical properties of K_6NaAsX_2 (X = Cl, Br, I), summarized in Table 4, were evaluated using standard elastic relations. Among the three compounds, $K_6NaAsCl_2$ exhibits lower values of shear modulus (G) and Young's modulus (Y), indicating reduced stiffness and a lower resistance to plastic deformation compared to $K_6NaAsBr_2$ and K_6NaAsI_2.

Cauchy's pressure, defined as the difference between the elastic constants $C_{12} - C_{44}$, provides insight into a material's ductility. Positive values generally indicate ductile behavior, whereas negative values suggest brittleness. As shown in Table 4, the positive Cauchy's pressure values for K_6NaAsX_2 (X = Cl, Br, I) confirm the ductile nature of these compounds.[77]

The shear constants, which serve as critical indicators of a material's dynamic stability, exhibit positive values for $K_6NaAsCl_2$, $K_6NaAsBr_2$, and K_6NaAsI_2, as reported in Table 4. These results confirm the mechanical stability of the compounds.

Additionally, anisotropic parameters such as the Zener anisotropy index (A_Z) and the Universal anisotropy index (A^U) were calculated using the second-order elastic constants (SOECs),[82,83] as presented in Table 4. For isotropic materials, A_Z equals 1, indicating a uniform shear response. Any deviation from unity, as observed in the computed A_Z and A^U values, confirms the anisotropic nature of K_6NaAsX_2 (X = Cl, Br, I). Furthermore, the elastic constants were used to compute the Kleinman parameter (ξ), reported in Table 5. The relatively low values of ξ indicate that these materials exhibit high resistance to bond angle distortions and bond bending.[77]

Table 5 Thermodynamic parameters for K_6NaAsX_2 (X = Br, Cl)

Parameters	$K_6NaAsCl_2$	$K_6NaAsBr_2$	K_6NaAsI_2
v_t (ms^{-1})	1547.29	1589.10	1479.74
v_l (ms^{-1})	2852.04	2728.81	2554.71
v_m (ms^{-1})	1685.86	1712.90	1596.52
θ_D (K)	90.79	98.52	96.93
ω_D (THz)	74.91	81.32	80.02
H_v (GPa)	0.002	0.003	0.003
T_m (K)	652.28	634.75	653.67

3.10 Thermal properties

Understanding thermodynamic properties is crucial for improving energy conversion efficiency in solar cells and other photovoltaic devices. To investigate these characteristics, simulations were performed on K_6NaAsX_2 (X = Cl, Br, I) at high temperatures and constant pressure using the quasi-harmonic Debye approximation, based on their ground-state structural parameters. This approach allowed the evaluation of essential thermodynamic parameters relevant to optoelectronic performance.

The overall efficiency of solar cells depends on key factors such as short-circuit current, open-circuit voltage, and energy conversion efficiency. Thermodynamic quantities, including average sound velocity (v_m), Vickers hardness (H_V), melting temperature (T_m), Debye temperature (θ_D), and Debye frequency (ω_D), play a critical role in optimizing materials for such applications.[84] Given that solar devices often operate under harsh conditions, thermodynamic stability is a key criterion for material selection. As shown in Table 5, increasing the halogen atom's atomic number in K_6NaAsX_2 (X = Cl, Br, I) leads to a systematic increase in parameters such as transverse sound velocity, reflecting predictable trends in physical behavior due to halogen substitution. Among these parameters, the Debye temperature (θ_D) is particularly significant, as it reflects the strength of atomic bonding and directly influences elasticity, heat capacity, and melting point. Higher θ_D values indicate stronger bonding, improved thermal conductivity, and greater thermal stability. The θ_D values for the studied compounds, derived from average sound velocities, are summarized in Table 5.

This calculation is based on key physical constants, including Planck's constant $\left(\hbar = \frac{h}{2\pi}\right)$, Boltzmann's constant ($K_B$), and Avogadro's number (N_A), as well as the total number of atoms in the compound (N) and the average acoustic sound velocity (v_m). These parameters are incorporated into the relevant equations to evaluate the thermodynamic properties.[77]

During solar cell fabrication, materials are often exposed to high temperatures, particularly during processes such as crystalline silicon growth or metal contact formation. Therefore, the melting temperature of a material is a critical parameter. A low melting point may lead to deformation, cracking, or melting, which can negatively impact device performance and reliability. Conversely, an excessively high melting point can complicate processing and increase manufacturing costs. The elastic constant C_{11} is frequently used to estimate a material's melting temperature,[85] providing valuable insight into its thermal

stability and suitability for high-temperature solar cell fabrication.[77]

The melting temperatures of the proposed compounds are listed in Table 5. Among them, K_6NaAsI_2 exhibits the highest melting point (653.67 K), followed by $K_6NaAsCl_2$ (652.28 K) and $K_6NaAsBr_2$ (634.75 K), indicating stronger atomic bonding in the iodine-based compound. The Debye frequency, ω_D, which represents the maximum vibrational frequency that phonons can attain during heat transfer, is another key parameter for assessing thermal behavior. Additionally, the Vickers hardness (H_V) and ω_D of these compounds were calculated using established theoretical models.[86]

These properties provide valuable insights into the mechanical strength and thermal stability of the materials. As shown in Table 5, the Debye temperature, Debye frequency, melting temperature, and hardness all increase with the atomic number of the halogen, reflecting stronger atomic bonding and greater thermal durability across the series.

4. Conclusion

In this study, density functional theory (DFT) was employed to investigate the structural, electronic, optical, elastic, thermoelectric, thermodynamic, photovoltaic, and photocatalytic properties of novel double antiperovskites (DAP) K_6NaAsX_2 (X = Cl, Br, I) using the FP-LAPW + lo method (WIEN2k). Structural optimizations were performed with WC-GGA and found that the lattice constants are 12.65 Å ($K_6NaAsCl_2$), 12.66 Å ($K_6NaAsBr_2$) and 12.72 Å (K_6NaAsI_2) which are greater than previously studied $K_2NaAsCl_6$ (10.31 Å). By calculating the bandgap of all materials, we observe that these materials have small values of the bandgap without incorporatin spinorbit coupling (SOC) which are 0.62 eV ($K_6NaAsCl_2$), 0.61 eV ($K_6NaAsBr_2$) and 0.60 eV (K_6NaAsI_2). These values of the bandgap are further decreased on applying SOC from 0.62 eV to 0.58 eV for $K_6NaAsCl_2$, 0.61 to 0.57 eV for $K_6NaAsBr_2$ and 0.60 eV to 0.54 eV for K_6NaAsI_2. By applying modified Beck–Johnson approximation (mBJ) along with SOC (Hybrid calculation), we obtained direct bandgap of 1.48 eV for $K_6NaAsCl_2$ (3.52 eV for $K_2NaAsCl_6$), 1.34 eV ($K_6NaAsBr_2$) and 1.16 eV (K_6NaAsI_2). DOS analysis elucidated the orbital contributions close to the Fermi level from which As-p orbital has maximum contribution in valence band than others and K-p orbital has maximum the highest contribution in conduction band in all studied materials. Optical properties, including refractive index, absorption, reflectivity, and optical conductivity, were presented. These results show that $K_6NaAsCl_2$ has the highest absorption of 3.2×10^5 cm^{-1} at 2.86 eV (433.51 nm). Effective mass of electron m_e^* for (K_6NaAsX_2) (X = Cl, Br, I) 0.32, 0.12 and 0.03 respectively which are less than that of Si (1.09) respectively, therefore it is expected that the carrier mobility of these materials is greater than Si which is strongly demanded for optoelectronic devices. Thermoelectric properties show that $K_6NaAsCl_2$ has *ZT* of 0.77 at 300 K and crosses 0.8 at 900 Kwhich is greater than reported double perovskite $K_2NaAsCl_6$ (0.11). Calculated elastic constants confirm mechanical stability, while thermodynamic parameters such as C_P, C_V, enthalpy, Gibbs free energy, and TS were computed. The values for C_P and C_V for all materials increase abruptly upto 200 K while gradually increases from 200 K to 1000 K. According to standard SLME analysis, the SLME efficiencies of the material under study were 6.82%, 7.34%, and 7.73% for K_6NaAsX_2 (X = Cl, Br, I) at 0.5 μm thick layer, respectively. The band-edge alignment of the all studied DAP compounds show good response for oxidation relative to the water-splitting redox potentials across pH values from 0 to 7. These DAP demonstrate potential for optoelectronic applications and solar water-splitting due to their optimal bandgaps and strong photocatalytic activity.

Conflicts of interest

The authors declare that they have no known competing financial interests or personal relationships that could have appeared to influence the work reported in this paper.

Data availability

Data will be made available on request.

Acknowledgements

The authors extend their appreciation to Ongoing Research Funding program - Research Chairs (ORF-RC-2025-5522), King Saud University, Riyadh, Saudi Arabia. The author Y. Saeed would like to thank Higher Education Commission (HEC) of Pakistan for providing grant under NRPU-15844.

References

1 T. Wu, M. L. Yao and M. Q. Long, First principle calculations of interface interactions and photoelectric properties of perovskite $CsPbX_3$ (X = Cl, Br, I) and penta-graphene van der Waals heterostructures, *Acta Phys. Sin.*, 2021, **70**, 056301.
2 H. K. Ting, L. Ni, S. B. Ma, Y. Z. Ma, L. X. Xiao and Z. J. Chen, Progress in electron-transport materials in application of perovskite solar cells, *Acta Phys. Sin.*, 2015, **64**, 038802.
3 P. Zhao, J. Su, Y. J. Guo, L. Wang, Z. H. Lin, Y. Hao, X. P. Ouyang and J. J. Chang, Cs_2TiI_6: a potential lead-free all-inorganic perovskite material for ultrahigh-performance photovoltaic cells and alpha-particle detection, *Nano Res.*, 2022, **15**, 2697–2705.
4 Y. Guo, Y. B. Xue and L. Q. Xu, Interfacial interactions and enhanced optoelectronic properties of GaN/perovskite heterostructures: insight from first-principles calculations, *J. Mater. Sci.*, 2021, **56**, 11352–11363.
5 G. M. Sui, G. J. Yan, G. Yang, B. Zhang and Y. Q. Feng, Theoretical investigation on structure and optoelectronic performance of two-dimensional fluorbenzidine perovskites, *Acta Phys. Sin.*, 2022, **71**, 208801.
6 D. Wang, H. M. Zhu, Z. M. Zhou, Z. W. Wang, S. L. Lv, S. P. Pang and G. L. Cui, Effect of solvent on the perovskite thin film morphology and crystallinity, *Acta Phys. Sin.*, 2015, **64**, 038403.

7 Y. B. Fu, H. Wei, L. Wei, H. D. Zhang, X. P. Wang, B. Liu, Y. Y. Zhang, X. S. Lv, J. X. Zhou and H. J. Yu, Origin of the difference in thermal conductivity and anharmonic phonon scattering between $LiNbO_3$ and $LiTaO_3$, *CrystEngComm*, 2021, **23**, 8572–8578.

8 Y. N. Xiao, P. F. Sui, Y. C. Zhao, J. Ni, S. Meng and Z. H. Dai, Low lattice thermal conductivity of hydride-based cubic antiperovskites A_3HB (A = Li, Na; B = S, Se, Te) with higher-order anharmonicity correction, *Int. J. Energy Res.*, 2022, **46**, 13687–13697.

9 Y. Liu, L. H. Ni, G. Xu, C. L. Song, G. R. Han and Y. Zheng, Phase transition in $PbTiO_3$ under pressure studied by the first-principles method, *Physica B*, 2008, **403**, 3863–3866.

10 D. Han, C. B. Feng, M. H. Du, T. Zhang, S. Z. Wang, G. Tang, T. Bein and H. Ebert, Design of high-performance lead-free quaternary antiperovskites for photovoltaics via ion type inversion and anion ordering, *J. Am. Chem. Soc.*, 2021, **143**, 12369–12379.

11 J. Chen, X. Cai, D. Yang, D. Song, J. Wang, J. Jiang, A. Ma, S. Lv, M. Z. Hu and C. Ni, Recent progress in stabilizing hybrid perovskites for solar cell applications, *J. Power Sources*, 2017, **355**, 98–133.

12 M. J. Fang, C. W. Tsao and Y. J. Hsu, Semiconductor nanoheterostructures for photoconversion applications, *J. Phys. D: Appl. Phys.*, 2020, **53**, 143001–143026.

13 Y. H. Chiu, T. H. Lai, M. Y. Kuo, P. Y. Hsieh and Y. J. Hsu, Photoelectrochemical cells for solar hydrogen production: Challenges and opportunities, *APL Mater.*, 2019, **7**, 080901–080911.

14 N. Erum, R. Sharma, A. Kumar, J. Nanda, R. Ghodhbani and N. Kamolova, Probing the physical properties of novel lead-free double perovskites $A_2NaAsCl_6$ (A = K and Rb): A first-principles approach, *New J. Chem.*, 2025, **49**, 11010–11021.

15 M. Z. Rehman, S. A. M. Abdelmohsen, E. A. Mahmoud, M. U. Saeed, M. Idrees, M. Shafiq, B. Amin and Y. Saeed, First principles study of structural, electronic, elastic and optical properties of $Cs_2LiTlBr_6$ and $Cs_2NaTlBr_6$, *Mater. Sci. Semicond. Process.*, 2022, **151**, 106993.

16 U. Rani, P. K. Kamlesh, R. Agarwal, J. Kumari and A. S. Verma, Electronic and thermo-physical properties of double antiperovskites X_6SOA_2 (X = Na, K and A = Cl, Br, I): a non-toxic and efficient energy storage materials, *Int. J. Quantum Chem.*, 2021, **121**, 26759.

17 Y. Yu, Z. Wang and G. S. Shao, Theoretical design of double anti-perovskite Na_6SOI_2 as a super-fast ion conductor for solid Na^+ ion batteries, *J. Mater. Chem. A*, 2018, **6**, 19843–19852.

18 M. Mebrouki, T. Ouahrani and Y. O. Ciftci, Unraveling thermal and dynamical properties of the cubic $BaVO_3$ perovskite from first-principles calculation, *Int. J. Thermophys.*, 2016, **37**, 71–80.

19 K. Djebari, A. Dahani, M. Djermouni, K. Dine, A. Cherif, O. Arbouche, A. Zaoui and S. Kacimi, Spontaneous polarization study in $A^{3+}B^{4+}(O_2N)^{7-}$ and $A^{2+}B^{5+}(O_2N)^{7-}$ perovskite-type oxynitrides: a first principles investigation, *Appl. Phys. A*, 2022, **128**, 398–410.

20 Q. Gao, R. Y. Ma, L. Li, H. H. Xie, J. B. Deng and X. R. Hu, First-principle study on compensated half metallic double perovskite compound Ba_2PrVO_6, *J. Supercond. Novel Magn.*, 2017, **30**, 545–554.

21 H. X. Gao, D.-Y. Hu, T.-Y. Tang, Q.-Q. Liang, Q. Dai, S.-S. Wu and Y.-L. Tang, First-principles study on the structural, electronic, elastic, optical and thermodynamic properties of double antiperovskites X_6BiSbN_2 (X = Mg, Ca, Sr), *J. Phys. Chem. Solids*, 2004, **187**, 111859.

22 P. Blaha, K. Schwarz, G. K. H. Madsen, D. Kvasnicka, and J. Luitz, *WIEN2k; an Augmented Plane Wave Plus Local Orbital Program for Calculating Crystal Properties*, Vienna University of Technology, Austria, 2001.

23 Z. Wu and R. E. Cohen, More accurate generalized gradient approximation for solids, *Phys. Rev. B:Condens. Matter Mater. Phys.*, 2006, **73**, 235116.

24 J. P. Perdew, K. Burke and M. Ernzerhof, Generalized gradient approximation made simple, *Phys. Rev. Lett.*, 1996, **77**, 3865.

25 E. Engel and S. H. Vosko, Exact exchange-only potentials and the virial relation as microscopic criteria for generalized gradient approximations, *Phys. Rev. B:Condens. Matter Mater. Phys.*, 1993, **47**, 13164.

26 Z. Ali, I. Ahmed, I. Khan and B. Amin, Electronic structure of cubic perovskite $SnTaO_3$, *Intermetallics*, 2012, **31**, 287.

27 G. Murtaza, I. Ahmed, B. Amin and M. Zahid, Investigation of structural and optoelectronic properties of $BaThO_3$, *Opt. Mater.*, 2011, **33**, 553.

28 H. Jiang, Band gaps from the Tran-Blaha modified Becke-Johnson approach: A systematic investigation, *J. Chem. Phys.*, 2013, **138**, 134115.

29 J. A. Camargo-Martinez and R. Baquero, Performance of the modified Becke-Johnson potential for semiconductors, *Phys. Rev. B:Condens. Matter Mater. Phys.*, 2008, **86**, 195106.

30 R. A. Jishi, O. B. Ta and A. A. Sharif, Modeling of lead halide perovskites for photovoltaic applications, *J. Phys. Chem. C*, 2014, **118**, 28344–28349.

31 R. A. Jishi, Modifed Becke-Johnson exchange potential: improved modelling of lead halides for solar cell applications, *AIMS Mater. Sci.*, 2016, **3**, 149–159.

32 Y. Saeed, B. Amin, H. Khalil, F. Rehman, H. Ali, M. I. Khan, A. Mahmood and M. Shafiq, $Cs_2NaGaBr_6$: a new lead-free and direct bandgap halide double perovskite, *RSC Adv.*, 2020, **10**, 17444–17451.

33 C. Y. Wang, S. R. Li, S. F. Wang, P. X. Zhao, R. S. Zhuo and B. Y. Yu, Effect of biaxial Pre-proof strain on monolayer MoS_2 and its vacancy defect system: a first-principles study, *J. Solid State Chem.*, 2023, **317**, 123711.

34 M. A. Green, Intrinsic concentration, effective densities of states, and effective mass in silicon, *J. Appl. Phys.*, 1990, **67**, 2944–2954.

35 A. A. Emery and C. Wolverton, High-throughput DFT calculations of formation energy, stability and oxygen vacancy formation energy of ABO_3 perovskites, *Sci. Data*, 2017, **4**, 170153.

36 C. Li, X. Lu, W. Ding, L. Feng, Y. Gao and Z. Guo, Formability of ABX_3 (X = F, Cl, Br, I) halide perovskites, *Acta Crystallogr., Sect. B:Struct. Sci.*, 2008, **64**, 702–707.

37 J. Liang, C. Wang, Y. Wang, Z. Xu, Z. Lu, Y. Ma, H. Zhu, Y. Hu, C. Xiao, X. Yi, G. Zhu, H. Lv, L. Ma, T. Chen, Z. Tie, Z. Jin and J. Liu, All-inorganic perovskite solar cells, *J. Am. Chem. Soc.*, 2016, **138**, 15829–15832.

38 Z. Abbas, N. Jabeen, A. Hussain, F. Kabir, T. Alshahrani, H. H. Raza, S. Muhammad, S. Azam and I. Gorczyca, Effect of Nb, Ta and V replacements on electronic, optical and elastic properties of $NbCu_3Se_4$: a GGA+U study, *J. Solid State Chem.*, 2021, **301**, 122338.

39 P. Mondal, N. A. Shahed, S. Khanom, M. K. Hossain and F. Ahmed, Effect of oxygen defects in tuning the half-metallic and optical nature of Sr_2CoXO_6 (X = Mo and W): a first-principles study, *Mater. Chem. Phys.*, 2022, **277**, 125429.

40 L. D. Whalley, J. M. Frost, Y. K. Jung and A. Walsh, Perspective: Theory and simulation of hybrid halide perovskites, *J. Chem. Phys.*, 2017, **146**, 220901.

41 D. Y. Hu, X. H. Zhao, T. Y. Tang, L. Li, L. K. Gao and Y. L. Tang, First-principles calculations to investigate structural, elastic, electronic and optical properties of lead-free perovskite derivatives Cs_2SeX_6 (X = Cl, Br, I)" Optic, *Mater*, 2021, **119**, 111316.

42 L. Y. Gong, P. Zhang, Q. Chen, Z. H. Lou, J. Xu and F. Gao, First principles study of structure and property of Nb^{5+} doped $SrTiO_3$", *Acta Phys. Sin.*, 2021, **70**, 227101.

43 M. Born and E. Wolf, *Principles of Optics: Electromagnetic Theory of Propagation, Interference and Diffraction of Light*, 7th (expanded) edn, Cambridge University Press, Cambridge, 1999.

44 M. Fox, *Optical Properties of Solids*, 2nd edn, Oxford University Press, 2010.

45 W. F. Goh and W. E. Pickett, Topological and thermoelectric properties of double antiperovskite pnictides, *J. Phys.:Condens. Matter*, 2020, **32**, 345502.

46 C. Y. Wang, S. R. Li, S. F. Wang, P. X. Zhao, R. S. Zhuo and B. Y. Yu, Effect of biaxial[110] strain on monolayer MoS_2 and its vacancy defect system: a first-principles study, *J. Solid State Chem.*, 2023, **317**, 123711.

47 Z. Abbas, N. Jabeen, A. Hussain, F. Kabir, T. Alshahrani, H. H. Raza, S. Muhammad, S. Azam and I. Gorczyca, Effect of Nb, Ta and V replacements on electronic, optical and elastic properties of $NbCu_3Se_4$: a GGA+U study" J, *Solid State Chem.*, 2021, **301**, 122338.

48 P. Mondal, N. A. Shahed, S. Khanom, M. K. Hossain and F. Ahmed, Effect of oxygen defects in tuning the half-metallic and optical nature of Sr_2CoXO_6 (X = Mo and W): a first-principles study, *Mater. Chem. Phys.*, 2022, **277**, 125429.

49 S. Berri, Theoretical analysis of the structural, electronic and optical properties of tetragonal Sr_2GaSbO_6, *Chin. J. Phys.*, 2017, **55**, 2476–2483.

50 M. Maglione and M. A. Subramanian, Dielectric and polarization experiments in high loss dielectrics: A word of caution, *Appl. Phys. Lett.*, 2008, **93**, 032902.

51 L. Jin, F. Li and S. Zhang, Decoding the fingerprint of ferroelectric loops: comprehension of the material properties and structures, *J. Am. Ceram. Soc.*, 2014, **97**, 1–27.

52 M. Barhoumi, I. Said, N. Sfina, N. K. Al-Saleem and T. Ghrib, A DFT study of the electronic and optical properties of four 2D thin films, *Mater. Chem. Phys.*, 2022, **286**, 126158.

53 P. Rani, G. S. Dubey and V. K. Jindal, DFT study of optical properties of pure and doped graphene, *Physica E*, 2014, **62**, 28–35.

54 K. Maeda and K. Domen, Photocatalytic water splitting: recent progress and future challenges, *J. Phys. Chem. Lett.*, 2021, **1**, 2655–2661.

55 R. M. Navarro Yerga, M. C. Alvarez Galvan, F. Del Valle, J. A. Villoria de la Mano and J. L. Fierro, Water splitting on semiconductor catalysts under visible-light irradiation, *ChemSusChem*, 2009, **2**, 471–485.

56 F. E. Osterloh, Inorganic materials as catalysts for photochemical splitting of water, *Chem. Mater.*, 2008, **20**, 35–54.

57 X. Hu, G. Li and J. C. Yu, Design, fabrication and modification of nanostructured semiconductor materials for environmental and energy applications, *Langmuir*, 2010, **26**, 3031–3039.

58 A. Kudo, Photocatalysis and solar hydrogen production, *Pure Appl. Chem.*, 2007, **79**, 1917–1927.

59 M. U. Saeed, T. Usman, S. Pervaiz, Z. Ali, Y. M. Alanazi, A.-U.-R. Bacha and Y. Saeed, DFT analysis of alkali scandium sulfides $AScS_2$ (A = K, Rb): Unveiling structural, electronic, and optical properties for enhanced photocatalysis, *ACS Appl. Opt. Mater.*, 2024, **2**, 1955–1964.

60 J. Liu, X. Fu, S. Chen and Y. Zhu, Electronic structure and optical properties of Ag_3PO_4 photocatalyst calculated by hybrid density functional method, *Appl. Phys. Lett.*, 2011, **99**, 191903.

61 M. Saeed, I. U. Haq, A. S. Saleemi, S. U. Rehman, B. U. Haq, A. R. Chaudhry and I. Khan, First-principles prediction of the ground-state crystal structure of double-perovskite halides Cs_2AgCrX_6 (X = Cl, Br, and I), *J. Phys. Chem. Solids*, 2022, **160**, 110302.

62 T. A. Pham, D. Lee, E. Schwegler and G. Galli, Interfacial effects on the band edges of functionalized Si surfaces in liquid water, *J. Am. Chem. Soc.*, 2014, **136**, 17071–17077.

63 X. Li, J. Yu, J. Low, Y. Fang, J. Xiao and X. Chen, Engineering heterogeneous semiconductors for solar water splitting, *J. Mater. Chem. A*, 2015, **3**, 2485–2534.

64 M. U. Saeed, T. Usman, S. M. Ali, S. Pervaiz, H. O. Elansary, I. M. Moussa, M. A. El-Sheikh, A.-U.-R. Bacha and Y. Saeed, Exploring electronic, optical, elastic, and photocatalytic properties in new double perovskites $Cs_2TlSbCl_6$ and $Cs_2TlBiCl_6$ materials: A GGA+SOC and hybrid functional study, *J. Mater. Res.*, 2024, **39**, 3155–3165.

65 J.-C. Zheng, Recent advances on thermoelectric materials, *Front. Phys.*, 2008, **3**, 269.

66 D. T. Morelli and G. A. Slack, High lattice thermal conductivity solids, in *High Thermal Conductivity Materials*, Springer, 2006, vol. 1, pp. 37–68.

67 G. L. Menaria, U. Rani, P. K. Kamlesh, R. Singh, M. Rani, N. Singh, D. C. Sharma and A. S. Verma, Electro-optic and transport properties with stability parameters of cubic KMgX (X = P, As, Sb, and Bi) half-Heusler materials: Appropriate for green energy applications, *Mod. Phys. Lett. B*, 2024, **245**, 2450283.

68 S. Y. Yue, T. Xu and B. Liao, Ultralow thermal conductivity in a two-dimensional material due to surface-enhanced resonant bonding, *Mater. Today Phys.*, 2018, **7**, 89–95.

69 G. L. Menaria, U. Rani, P. K. Kamlesh, M. Rani, N. Singh, D. C. Sharma and A. S. Verma, Comprehensive theoretical investigation of NaAlX (X = C, Si, and Ge) half-Heusler compounds: Unveiling the multifaceted properties for advanced applications, *Int. J. Mod. Phys. B*, 2024, **255**, 2550052.

70 N. V. Prabhu and K. A. Sharp, Heat capacity in proteins, *Annu. Rev. Phys. Chem.*, 2005, **56**, 521.

71 Q. Gao, R. Y. Ma, L. Li, H. H. Xie, J. B. Deng and X. R. Hu, First-principle study on ompensated half metallic double perovskite compound Ba_2PrVO_6, *J. Supercond. Novel Magn.*, 2017, **30**, 545–554.

72 Z. Huang, C. He, X. Qi, H. Yang, W. Liu, X. Wei, X. Peng and J. Zhong, Band structure engineering of monolayer MoS_2 on h-BN: first-principles calculations, *J. Phys. D: Appl. Phys.*, 2014, **47**, 075301.

73 R. M. Abraham, J. alvarez-Muniz, C. A. Arguelles, A. Ariga, T. Bostan, M. Bustamante and A. Camming, Tau neutrinos in the next decade form GeV to EeV, *J. Phys. G: Nucl. Part. Phys.*, 2022, **49**, 110501.

74 A. A. Baloch, M. I. Hossain, N. Tabet and F. H. Alharbi, Practical efficiency limit of methylammonium lead iodide perovskite solar cells, *J. Phys. Chem.*, 2018, **9**, 426–434.

75 J. Li and H. Chen, First-principles investigation of the mechanical and thermodynamic properties of the antiperovskite centrosymmetric platinum-based superconductors APt_3P (A = Ca, Sr, La and Ce), *Physica B*, 2020, **577**, 411791.

76 M. Y. Rudysh, M. Piasecki, G. L. Myronchuk, P. A. Shchepanskyi, V. Y. Stadnyk, O. R. Onufriv and M. G. Brika, $AgGaTe_2$ The thermoelectric and solar cell material: structure, electronic, optical, elastic and vibrational features, *Infrared Phys. Technol.*, 2020, **111**, 103476.

77 B. Asghar, M. U. Saeed, L. Sajid, S. Pervaiz, S. Khan, Z. Ali, A. Khan, Z. Ullah, H. O. Elansary and Y. Saeed, Ab-initio study of electronic, elastic, and optical properties of double antiperovskite, Li_6AgBiX_2 (X = Cl, Br, I), *Chem. Phys. Lett.*, 2025, **844**, 141900.

78 B. T. Wang, W. X. Zhang and W. D. Li, Mechanics, Lattice dynamics, and chemical bonding in ZrB_2 and ZrB_2 from first-principles calculations, *Sci. Adv. Mater.*, 2013, **5**, 1916–1921.

79 X. H. Zhao, Y. L. Tang, T. Y. Tang, X. F. Diao, L. K. Gao, Q. Xie, B. Shi, L. Yuan and L. M. Lu, Study on mechanical, electronic and optical properties of Pb-free double halide perovskites In_2TiX_6 (X = Cl, Br, I) for solar cells based on first-principles, *Mater. Today Commun.*, 2021, **26**, 102180.

80 L. K. Gao, X. H. Zhao, X. F. Diao, T. Y. Tang and Y. L. Tang, First-principles study of photoelectric properties of $CsSnBr_3$ under hydrostatic pressure, *Acta Phys. Sin.*, 2021, **70**, 158801.

81 J. Li and H. Chen, First-principles investigation of the mechanical and thermodynamic properties of the antiperovskite centrosymmetric platinum-based superconductors APt_3P (A = Ca, Sr, La and Ce), *Physica B*, 2020, **577**, 411791.

82 S. I. Ranganathan and M. Ostoja-Starzewski, Universal elastic anisotropy index, *Phys. Rev. Lett.*, 2008, **101**, 055504.

83 S. F. Pugh, XCII. Relations between the elastic moduli and the plastic properties of polycrystalline pure metals, *Philos. Mag.*, 1954, **45**, 823.

84 M. A. Rehman, J. U. Rehman and M. B. Tahir, Density functional theory study of structural, electronic, optical, mechanical, and thermodynamic properties of halide double perovskites Cs_2AgBiX_6 (X = Cl, Br, I) for photovoltaic applications, *J. Phys. Chem. Solids*, 2023, **181**, 111443.

85 M. Hattab and K. Rahmani, Thermodynamic, optical, and morphological studies of the Cs_2AgBiX_6 double perovskites (X = Cl, Br, and I): Insights from DFT study, *J. Alloys Compd.*, 2023, **960**, 170650.

86 S. A. Dar, R. Sharma, V. Srivastava and U. K. Sakalle, Investigation on the electronic structure, optical, elastic, mechanical, thermodynamic and thermoelectric properties of wide band gap semiconductor double perovskite Ba_2InTaO_6, *RSC Adv.*, 2019, **9**, 9522–9532.